First results from SAPAC: towards a 3D-picture of the Fornax cluster core¹

Laura P. Dunn and

Helmut Jerjen

Research School of Astronomy and Astrophysics, Mt Stromlo Observatory, Australian National University, Cotter Road, Weston ACT 2611 Australia

laurad@mso.anu.edu.au, jerjen@mso.anu.edu.au

ABSTRACT

A sophisticated SBF analysis package has been developed, designed to measure distances of early-type galaxies by means of surface brightness fluctuations of unresolved stars. This suite of programs called SAPAC is made readily available to the astronomical community for extensive testing with the long-term goal to provide the necessary tools for systematic distance surveys of early-type galaxies using modern optical/NIR telescopes equipped with wide-field cameras. We discuss the technical and scientific concepts of SAPAC and demonstrate its capabilities by analysing deep B and R-band CCD images of 10 dwarf elliptical (dE) galaxy candidates in the Fornax cluster obtained with FORS1 at the VLT. All candidates are confirmed as cluster members. We then turn our attention to the innermost region of the Fornax cluster. A total of 29 early-type galaxies closer than three cluster core radii (2°) from the central galaxy NGC1399 have radial velocities and SBF distances. Their Hubble diagram exhibits a pronounced Sshaped infall pattern suggesting a picture that Fornax is still in the process of formation during the present epoch through a general collapse and possible accretion of distinct groups of galaxies. From fitting a model we estimate the cluster mass within 720 kpc projected distance from NGC1399 which is $2.3 \pm 0.3 \times 10^{14} \mathcal{M}_{\odot}$. The associated collapse time is $t_{\text{collapse}} = 2.9^{+1.6}_{-0.9} \,\text{Gyr}$. After cleansing our galaxy sample from a few kinematical outliers the true distance of the Fornax cluster core is determined at $20.13\pm0.40\,\mathrm{Mpc}$ [$(m-M)_0=31.51\pm0.04\,\mathrm{mag}$]. Applying a bootstrap resampling technique on the distance distribution with individual distance errors taken into account further reveals a small intrinsic cluster depth of $\sigma_{\rm int} = 0.74^{+0.52}_{-0.74}\,{\rm Mpc}$ in best agreement with the cluster's linear extension in the sky: $\sigma_{\rm R.A} = \sigma_{\rm DEC} \approx 0.5\,{\rm Mpc}$. We conclude that the early-type galaxy population in the Fornax cluster must be spatially well constrained with no evidence of elongation along the line-of-sight in contrast to the Virgo cluster. Moreover, we find marginal evidence for substructure, a results that is consistent with the young evolutionary state of the cluster and the overall galaxy infall. Combining the kinematically defined cluster distance with the mean cosmological velocity for the central cluster galaxy sample yields a Hubble constant of $H_0 = 63 \pm 5\,{\rm km\,s^{-1}\,Mpc^{-1}}$.

Subject headings: galaxies: clusters: individual(Fornax) – galaxies: distances and redshifts – galaxies: dwarf – galaxies: elliptical and lenticular, cD – methods: data analysis

1. Introduction

Finding low star density dwarf galaxies in the local Universe is, by nature, a challenging task. Over the last two decades, numerous surveys (e.g. Binggeli et al. 1985; Jerjen & Dressler 1997; Ferguson & Sandage 1990; Jerjen et al. 2000a; Karachentsev et al. 1995; Caldwell et al. 1998) have produced hundreds of candidates in nearby groups and clusters based on morphological properties. But due to the lack of any distance information large numbers still remain only dwarf candidates today.

To separate the wheat from the chaff, i.e., genuine dwarf galaxies from similar looking background spirals and giant ellipticals, distances are required. The importance of distances, however, extends far beyond the unambiguous identification and spatial location of new dwarf galaxies. The careful construction of highly complete, volume-limited galaxy samples like the 10 Mpc sphere (Kraan-Korteweg & Tammann 1979; Schmidt & Boller 1992; Karachentsev et al. 2004) yields the exact number and distribution of dwarfs relative to larger galaxies and provides crucial empirical input to better constrain theories of galaxy formation, including the faint-end of the galaxy luminosity function and the merging rate (Tully et al. 2002; Jerjen et al. 2004b). Furthermore, accurate distances permit studies of the dwarf galaxy distribution in 3-D and, if combined with kinematical and stellar population data, provide insight into the importance of environmentally driven over self-induced physical processes that govern dwarf galaxy evolution (e.g. Peebles et al. 2001).

¹Based on observations collected at the ESO-VLT, under program ESO 68.A-0176

Unlike the scarcely evolved, low density environment populating dwarf irregular galaxies, dwarf elliptical (dE) galaxies are lacking significant amounts of neutral hydrogen gas preventing a relatively simple distance estimate via 21cm redshift. Furthermore, little help is coming from empirical scaling relations between galaxy luminosity and surface brightness (Binggeli & Cameron 1991) or Sérsic shape parameter (Binggeli & Jerjen 1998) as the large intrinsic scatter turns out to be unsuitable for individual distance measurements. That is why in the last decade a formidable observational effort has been devoted to deriving distances to dEs by using the tip magnitude of the red giant branch (TRGB), a powerful Pop II distance indicator (Karachentsev et al. 2003; Da Costa & Armandroff 1990, and references therein). However, the requirement of accurate photometry for individual stars 1–2 magnitudes below the tip $[m_I \geq 25.8 + 5 \log(D/5 \text{Mpc})]$ at distance D[Mpc] sets a practical application limit at $\approx 5 \text{ Mpc}$ beyond which TRGB measurements quickly become very costly and time consuming. This was demonstrated by Harris et al. (1998) who spent nine hours with the HST to obtain the TRGB distance for a single dE galaxy (IC3388) in the Virgo cluster.

Because of this limitation, a new distance indicator, the so-called surface brightness fluctuation (SBF) method, has received increasing attention in recent years. The method quantifies the statistical pixel-to-pixel variation of star counts across a galaxy image with the major technical advantage of working on unresolved stellar populations. Ground-based CCD images with relatively short exposure times can be used instead of high resolution space-based observations making the SBF method extremely efficient. Distance measurements for early-type galaxies far beyond the reach of any other distance indicator become possible.

The theoretical framework of the SBF method was developed by Tonry & Schneider (1988) to study the distribution of luminous giant ellipticals in the local Universe (e.g. Tonry et al. 2001). While SBF applications were initially focused on high surface brightness systems (Ajhar & Tonry 1994; Jensen et al. 1996; Thomsen et al. 1997), Jerjen and collaborators (Jerjen et al. 1998, 2000b, 2001; Jerjen 2003) demonstrated that the method works equally well for dEs with stellar surface densities as low as $\mu_{\rm B_{eff}} = 26\,{\rm mag\,arcsec^{-2}}$ and luminosities comparable to Local Group dwarfs like Leo I, And II, and Sculptor ($M_B = -10\,{\rm mag}$). The SBF method has since been successfully applied to dwarf candidates in the distance range from 10–40 Mpc, employing 2-m ground-based telescopes (Rekola et al. 2005), the 8-m ESO-VLT (Mieske & Hilker 2003; Jerjen et al. 2004a), and the HST (Jordán & Null 2005; Mei et al. 2005).

Noticing that dE galaxies are by far the most numerous galaxy type at the current cosmological epoch (Ferguson & Binggeli 1994), the SBF technique, in combination with modern wide-field imaging at optical and near-IR telescopes like SUBARU, VISTA, and

LSST, has the potential to play a major role in future distance surveys of early-type galaxies in the local Universe. Using extended source catalogues from SDSS and Pan-STARRS in the North and SkyMapper in the South there is the prospect of carrying out SBF distance surveys in a similar fashion as redshift surveys are done today. For the efficient processing of such large amount of imaging data we are currently engaged in a project of developing an automated SBF Analysis Pipeline for the Astronomical Community called SAPAC.

In §2 we will introduce SAPAC, discuss the data requirements for the pipeline and give an overview of the SBF method. We will then demonstrate its capabilities in §3 by processing VLT+FORS1 CCD images for 10 Fornax cluster dE candidates of similar quality as existing and future survey telescopes are expected to produce. In §4 we endeavor to extract clues about the 3-D cluster structure from the spatial distribution of early-type galaxies in the central region of Fornax. Combining galaxy velocities and distances and analysing the Hubble diagram enables the measurement of various cluster parameters such as the total mass and dynamical collapse time, as well as a value for the Hubble constant. We summarize our results in §5.

2. SAPAC description

Previous SBF measurements have entailed individuals hand selecting regions in galaxy images for the analysis. To make the data reduction more efficient and results as impartial as possible we have developed a rapid and easy-to-use visual SBF tool. SAPAC² is a software package that addresses the entire SBF analytical process from galaxy modeling and Fourier analysis to fluctuation magnitude calibration and presentation of the distance results. It works on any pair of CCD images that meets four basic criteria as discussed in the following paragraph. SAPAC currently runs under Linux but will be made available for other operating systems in the near future. It comprises of a suite of Perl scripts using an IRAF module Astro::IRAF::CL³ and a sophisticated graphical user interface, also written in Perl, employing Tk⁴. For more information on the computing requirements to run the software we refer to the SAPAC manual.

²http://www.mso.anu.edu.au/~laurad/sapac

 $^{^3}$ http://search.cpan.org/ \sim sjquinney/Astro-IRAF-CL-0.2.0/CL.pm

⁴http://search.cpan.org/~ni-s/Tk/

2.1. Data Requirements

There are four checks that help the SAPAC user to decide whether a set of CCD images of a galaxy are suitable for the SBF analysis. They are as follows:

Galaxy morphology: the galaxy light distribution must be overall radially symmetric and have minimal structure to permit accurate 2-D modeling. This technical constraint basically restricts the application to early-type galaxies and bulges of spiral galaxies. We like to note that sophisticated galaxy fitting programs such as galfit (Peng et al. 2002) can actually successfully model entire spiral galaxies. But even so, the SBF signal depends on the star formation history, age, and metallicity of the underlying stellar population and thus is less constrained for spiral than for elliptical galaxies. Working with a more complex parameter space leads to a larger scatter in the calibration of the SBF method. Hence, there is a stellar population argument too why an SBF analysis should be restricted to early-type galaxies, but this might change in the future.

Photometric bands: As the measured fluctuation magnitude is colour dependent calibrated CCD images in two different photometric bands are required, e.g. (B, R) or (g_{475}, z_{850}) .

Seeing: In essence, the CCD images must be obtained under good atmospheric conditions. A seeing value of 1 arcsec or better is recommended for the image used for the SBF analysis (i.e. R or z_{850}), but this depends on the angular size of the galaxy. A rule of thumb is $FWHM \leq r_{eff}["]/20$, where r_{eff} is the half-light radius of the galaxy. The image in the other photometric band can be of slightly lower quality but should not exceed 20-30 percent to remain immune to the effect of pixel smearing.

Integration time: the total integration time t for the image in the band used for the SBF analysis is estimated from five quantities:

- mean surface brightness of the galaxy (μ_{qal})
- surface brightness of the sky background (μ_{sky})
- \bullet distance modulus of the galaxy (DM)
- fluctuation luminosity of the underlying stellar population in the SBF band (\overline{M})
- photometric zero point of the telescope+instrument system, i.e. the magnitude of a star providing 1 ADU s⁻¹ on the CCD detector (m_1)

The integration time can then be expressed as a function of the signal-to-noise ratio S/N in the derived SBF power spectrum (see §2.2):

$$t = S/N \cdot 10^{0.4(\mu_{gal} - \mu_{sky} + DM + \overline{M} - m_1)}$$
 (1)

Fig.1 illustrates Eq.1, plotting signal-to-noise versus integration time for different values of μ_{gal} . This example is tuned for an old, metal-poor stellar system ($\overline{M}_R = -1.30 \,\mathrm{mag}$) at the tentative distance modulus of 31.50 mag, observed in the R-band with the VLT at no moon condition ($m_{1,R} = 27.10 \,\mathrm{mag}$, $\mu_{sky,R} = 20.8 \,\mathrm{mag\,arcsec^{-2}}$). From experience, a SBF distance can be derived reliably when the offset between shot noise level and SBF signal at wave number k = 0 is 0.5 dex or higher (see Rekola et al. 2005, Fig. 8). To achieve the equivalent S/N=3 in the power spectrum, the minimum integration time for a Fornax cluster dE with $\mu_{gal} = 24.5 \,\mathrm{mag\,arcsec^{-2}}$ is 1600 seconds. This is a factor 20 shorter that the 32,000 seconds spent by Harris et al. (1998) to measure the TRGB distance for the Virgo dwarf IC3388 with HST.

2.2. SAPAC outline

The SBF reduction pipeline follows the analysis steps as described by Jerjen et al. (2000b, 2001, 2004a), i.e., galaxy modeling, SBF field selection, Fourier analysis, fluctuation magnitude calibration, estimate of fluctuation contributions from unwanted sources, distance measurement. All steps are combined into a single package with a graphical user interface that is designed to be easy-to-use for novices but is powerful enough for experienced users. The pipeline requires an astronomical imaging and data visualization application like DS9 (Joye & Mandel 2003) to be running and that the CCD data available meets the requirements outlined in the previous section. Although it is necessary to have observations in two bands to measure a distance, SAPAC can calculate the power spectra of selected galaxy fields on a single CCD frame. This is useful to test the quality of a image for the purpose of an SBF analysis and thus to decide whether applying for more observing time to get the missing second passband image would be productive.

Obviously, the CCD images must be photometrically calibrated and carefully sky-subtracted, and the photometric zero points available as keywords in the fits headers. Furthermore, the two images must be on the same pixel scale and registered. Fig. 2 shows the steps by which the process follows for one of our observed galaxies FCC318.

2.2.1. Modeling the Light Distribution

The initial step in the SBF analysis process is to accurately model the light distribution of the galaxy (Fig. 2a) in both passbands. SAPAC finds the luminosity-weighted galaxy center from a user-defined square box and employing the IRAF command *imcentroid*. The IRAF procedure *ellipse* is used to generate the model which is subsequently subtracted from the original image. The best-fitting model and residual image for FCC318 is shown in Figs. 2b and 2c. The same modeling constraints are used on the second image. The 2-D modeling of the light distribution is a crucial step in preparation for the SBF analysis as any residual may affect the final results. Consequently, this delicate part is currently the most interactive in the process. Although the original purpose of this part of the software is to fit galaxies, the algorithm can be also used in a broader context of morphology studies or for deblending objects.

2.2.2. Normalisation, Masking and PSF Analysis

In the next stage, the residual image of the SBF band from step one is divided by the square root of the model for flux normalisation and bright objects are masked out. The masking is done automatically by SAPAC at two separate cut-off levels. The first mask is applied to high pixel values with a large radius surrounding these peaks in order to remove bright foreground stars; the second mask is applied at a lower cut with a smaller radius to excise fainter foreground stars and background galaxies. If by chance a part of a galaxy is heavily masked it should be omitted for the SBF analysis. An example of the normalized, masked image is seen in Fig. 2d, with a grid overlaid which will be discussed in the next section.

The third step is concerning the reference star that is needed to determine the PSF convolved component in the power spectra of the SBF fields. A suitable star selected by the user should be bright and well isolated, such that light from the target galaxy is not affecting it. We also recommend that the star is relatively close to the galaxy so that the influence of possible spatial PSF variation across the CCD chip is kept to a minimum. The profile of the star is determined by fitting a point spread function model and this will be used for the decomposition of the galaxy power spectrum.

2.2.3. SBF field analysis

The fourth step gives the user the opportunity to define the number of square SBF fields and their approximate size. An area of the galaxy is selected over which the grid is placed, as seen in Fig.2d. Each field is then analysed individually. The analysis comprises of each of the fields being Fourier transformed and the azimuthally averaged power spectrum being computed. The power spectrum of the mask is subtracted to remove the effects of the masking from the analysis. SAPAC then fits a linear combination of the flux normalized and exposure time weighted PSF power spectrum of the star and a constant at the power spectrum of the SBF field $PS(k) = P_0 \cdot PS_{star}(k) + P_1$, demanding a least squares minimisation. Data points at low spatial frequencies ($k \leq 5$) are omitted as they are likely affected by imperfect galaxy model subtraction. The derived power, P_0 , is still mildly contaminated by a contribution of unresolved background galaxies $P_{\rm BG}$. To estimate this contribution SAPAC employs the Jensen et al. (1998) equation adjusted for the R-band (Jerjen et al. 2001). Another potential source of unwanted fluctuations are globular cluster systems. Although this is an important issue for giant ellipticals, contributions from globular clusters in dEs are negligible due to the very low GC numbers observed in dEs (Miller et al. 1998). The expected few would be excised during the masking process and hence no further correction on P_0 is applied.

When corrected for background galaxies and Galactic extinction, A_R , the amplitude P_0 relates to the fluctuation magnitude of the unresolved stars in the galaxy (R-band) as: $\overline{m}_{\rm stars} = m_1 - 2.5 \log_{10}((P_0 - P_{\rm BG})/t) - A_R$, where t is the exposure time and m_1 is the photometric zero-point. For the purpose of calibrating the derived fluctuation magnitude, the colour $(B - R)_0$ of each SBF field is finally calculated by SAPAC using the galaxy model in the second passband.

2.2.4. Calibration and distance measurement

A semi-empirical calibration of the fluctuation magnitude \overline{M}_R for the colour range $0.8 < (B-R)_0 < 1.5$ was established (Jerjen 2005) by combining observational results from 36 SBF fields in seven nearby dwarf galaxies (Jerjen et al. 2001; Rekola et al. 2005) with independent distance measurements available from TRGB (Karachentsev et al. 1999, 2000) or SBF (Tonry et al. 2001) and extending it with theoretical results from stellar population synthesis models by Worthey (1994) and evolutionary tracks from the Padova library (Bertelli et al. 1994). Two distinct relationships were found depending on composition, age, and metallicity of the underlying stellar population: a parabolic branch covering the colour range $0.8 < (B-R)_0 < 1.35$ and a linear branch covering $1.1 < (B-R)_0 < 1.5$. The

two calibration loci are described analytically by Eqs. (2)+(3) with an intrinsic scatter of 0.15 mag. Both are used by SAPAC for the distance measurement:

$$\overline{M}_R = 6.09(B - R)_0 - 8.94$$
 (2)

$$\overline{M}_R = 1.89[(B-R)_0 - 0.77]^2 - 1.39$$
 (3)

Future versions of SAPAC will have the SBF calibration for the Sloan filter z_{850} implemented as presented by Mei et al. (2005).

SAPAC analyses each field automatically but it will be up to the user to keep or discard results from individual fields for the distance determination. Two of the most common reasons for omitting fields are imperfection in the modeling, especially around the center of the galaxy or fields with a high percentage of masked pixels due to superimposed bright foreground stars. Once the user has decided on the fields to include in the distance measurement, the pipeline will output the power spectrum of each field, a plot of the selected fields over the galaxy, and will generate the best-fitting calibration diagram with the distance modulus and estimates error including uncertainties in photometric zero points, power spectrum fitting, sky level determination, and Galactic extinction. Examples of the output will be shown in the next section.

3. Testing the pipeline on Fornax cluster dE candidates

As an opportunity to test the performance of SAPAC we processed CCD images of ten dE candidates from the Fornax Cluster Catalog (FCC, Ferguson 1989). The basic properties of these galaxies are listed in Table 1, where Column (1) is the FCC number, (2) is the morphological type, (3) and (4) are RA and Declination for epoch J2000, (5) is the integrated B-magnitude, (6) is the heliocentric velocity, (7) and (8) are the Galactic extinction in the B and R-bands, references are listed below the table. The velocities available in the literature for eight of the ten galaxies suggest cluster membership but no distances were measured to date. FCC279 and FCC318 even lack a velocity.

3.1. Observations and Reduction

The FORS1 (FOcal Reducer/Low dispersion Spectrograph) at UT3 of the Very Large Telescope at ESO Paranal Observatory was used in service mode to obtain deep B and R-band images of the target galaxies. The CCD was read out by four amplifiers, each reading one quarter of the CCD, known as four-port mode. The galaxies were centered on one of these

four quadrants, thus leaving the remaining three empty and available to be used as night flats. Each galaxy, except FCC274, was observed in 3 sets of $500 \,\mathrm{s}$ exposures in the B-band and $700 \,\mathrm{s}$ exposures in the R-band, each with slightly different pointings. As the observing log in Table 2 shows, FCC274 only has one exposure in the R-band but since the seeing in that single frame was excellent (0.56'') we were able to continue with our analysis on this galaxy. Galaxies FCC245 and FCC252 were observed three times, totaling 9 observations, but this was due to poor photometric conditions on some nights. We chose to use only the three images from the night with the best photometric conditions.

The data was reduced using routines within IRAF⁵. The bias level was removed from each of the quadrants using the overscan regions and a masterbias that was created from bias frames taken before and after every observing night. Night flats were median-combined to create masterflats for each filter and subsequently the images were flatfield corrected.

A series of photometric standard stars (Landolt 1992) were observed in various passbands under different airmasses every night in service mode. Due to these frequent observations, trends for the colour terms and extinction coefficients at Paranal are accurately monitored and reported by the VLT Quality Control and Trending Services (Hanuschik & Silva 2002) at Garching. Table 3 shows the extinction coefficients for B (Column 2) and R (Column 3) bands and the colour term (Column 4) derived for each night (Column 1). These values and our own set of standard stars were used to determine the photometric zero points in Column 5 (see Table 3).

Using the *starfind*, *xyxymatch* and *imalign* commands all the images from a particular galaxy were aligned by matching the positions between 30 to 50 stars. Star-free areas distributed uniformly over the CCD image but away from the galaxy were selected for an accurate sky background determination. The sky subtracted images from the same passband were then median combined using *imcombine* and finally these master images were flux calibrated.

3.2. Distances derived using SAPAC

The SBF analysis of the 10 Fornax dE candidates listed in Table 1 was performed using SAPAC. The chosen SBF fields for two of the sample galaxies are shown in Fig. 3 for illustration purpose. As mentioned before, fields that were not included in the final analysis

⁵IRAF is distributed by the National Optical Astronomy Observatories, which is operated by the Association of Universities for Research in Astronomy, Inc., under contract with the National Science Foundation

were either the center fields, which had residual from the modeling and subtraction, or, as in the case of FCC207, a nearby star created difficulties in determining the center, or they were outer fields which had large amounts of masked areas or the fluctuation signals were too low, meaning poor fitting of the power spectrum.

Table 4, serving as an example, summarises the measured values in the SBF analysis for the two galaxies shown in Fig. 3, i.e. FCC222 and FCC243: galaxy name and SBF field ID (Column 1), the pixel size of the SBF fields (Column 2), m_1 , the magnitude of a star providing 1 ADU s⁻¹ on the CCD (Column 3), the mean galaxy surface brightness in ADU (Column 4), the sky surface brightness in ADU (Column 5), P_0 , the time normalized amplitude of the best fit at wavenumber k=0 with the error in brackets (Column 6), P_1 , the level of the scale free white noise component in the power spectrum (Column 7), the signal-to-noise where $S/N = (P_0 - P_{BG})/(P_1 + P_{BG})$ (Column 8), and the fractional amount of fluctuation from unresolved high redshift galaxies, P_{BG}/P_0 (Column 9). The S/N for all ten galaxies ranges from 2.9 to 15.0 with a median value of 6.8. Most of the fields have a contribution from the background galaxies between 3 and 5%, with the exception of FCC252 which has a significantly higher fraction, at 8-10%. The fluctuation magnitude \overline{m}_R^0 , corrected for the background galaxy component and foreground extinction (Schlegel et al. 1998), is listed for each field in column 3 of Table 5, again for the two selected galaxies. Column 4 of this table gives the measured $(B-R)_0$ colour for each field of each galaxy, also corrected for foreground extinction. The power spectrum for each selected field for FCC222 and FCC243 are shown in Fig. 3, where the layout of the power spectrum corresponds to the fields placed on the galaxy. We note that the level of the scale free white noise component in the power spectra, equivalent to the ratio of sky and galaxy surface brightness, varies as expected. It is the lowest in the galaxy center, where the surface brightness peaks, and is significantly higher in the outer fields, where the star density is low.

Table 6 lists the SBF distances for the 10 galaxies analysed, with two results for FCC207 and FCC318. The second result for both these galaxies arises from using the parabolic calibration branch as, due to the $(B-R)_0$ colours of the fields being close to the intercept of the two branches, both calibration branches provided appropriate fits. These results are graphically shown in Fig. 4, where 12 calibration graphs can be seen, referring to the 10 individual galaxies plus the 2 parabolic branch options, denoted by "P". As a first result, we find that the observed distance range of 17.5 Mpc < D < 23.8 Mpc confirms all sample Fornax dE candidates as cluster members including FCC279 and FCC 318 which do not have velocity measurements to date.

The error in the power spectrum fitting is between 2 and 11% for all galaxies. The remaining sources of errors are 2% for the PSF normalization, 1-2% for the variation in

shape of the stellar PSF over the CCD, 0.02 mag in R and 0.03 mag in B for the photometric calibration uncertainty and 16% error in foreground extinction (Schlegel et al. 1998). Hence the combined error for an individual \overline{m}_R^0 measurement is between 0.03 mag and 0.11 mag (Column 3 in Table 5). Column 4 shows the error in the local colour of each field and this was determined using errors in sky level measurements, photometric zero points and Galactic extinction.

4. Discussion

4.1. Distance distribution and Substructures

With the availability of significant numbers of distances for cluster galaxies true 3-D substructure studies in clusters have finally come of age. Most recent distance studies of the Virgo cluster have found extensive substructure (West & Blakeslee 2000; Solanes et al. 2002; Jerjen 2003). West & Blakeslee (2000) used SBF distance measurements from Tonry et al. (2001) to 14 elliptical galaxies in the northern part of the Virgo cluster to show a strong collinear arrangement in three dimensions, defining a principal axis between NGC4387 and NGC4660, otherwise known as cluster A (Binggeli et al. 1987). Cluster B is centered around M49 and these two major concentrations of the Virgo Cluster are thought to be surrounded by three galaxy clouds. Jerjen et al. (2004a) also used the SBF method to determine distances to 16 dE galaxies in the Virgo cluster and found first evidence for line-of-sight bimodality in cluster A, when combined with 24 ellipticals with SBF distances from Tonry et al. (2001) and Neilsen & Tsvetanov (2000). They concluded that the northern cluster A consists in fact of two dynamically distinct systems, a small group around M86 falling into the M87 subcluster from the back.

The Fornax cluster is less rich than Virgo and considered structurally to be less complex. It hosts about 350 likely cluster members (Ferguson 1989). They are essentially concentrated in one major component that is dominated by early-type galaxies (see Fig. 5). The cluster has a King profile core radius of $R_{\rm c}=0.67^{\circ}~(\simeq 0.24\,{\rm Mpc})$ and a center that almost exactly coincides with the location of the giant elliptical NGC1399 (Ferguson 1989). Approximately three degrees to the southwest lies a loose aggregate that is dominated by the peculiar Sa galaxy Fornax A (NGC1316) and composed of mainly late-type galaxies. In Ferguson's initial study, cluster membership and background objects were distinguished for the most part based on morphology. Subsequent spectroscopic surveys have reassigned a few members from likely membership to background status and vice versa and have also determined some previously unknown redshifts (Drinkwater & Gregg 1998; Schröder et al. 2001; Drinkwater et al. 2001b). Madore et al. (1999) measured a relatively smooth Gaussian velocity distribution with very

little substructure compared to Virgo. Drinkwater et al. (2001a) analysed redshifts of 108 Fornax cluster members, including 55 dwarfs, and found kinematical evidence for a large main concentration, centered around the velocity of NGC1399. The small second component around NGC1316 has a slightly higher ($\approx 100\,\mathrm{km\,s^{-1}}$) mean velocity suggesting an infall towards the cluster center from the near side. But all this substructure evidence is based on velocities only and thus does not provide a genuine three dimensional picture of the Fornax cluster.

Fornax was also subject to some initial distance work. The Cepheid distances of three spiral galaxies were measured, NGC1365 at $18.3\pm2.3\,\mathrm{Mpc}$, NGC1326A at $18.7\pm1.9\,\mathrm{Mpc}$ (Silbermann et al. 1999), and NGC1425 at $22.2\pm1.4\,\mathrm{Mpc}$ (Mould et al. 2000), only one of them (NGC1365) inside the central area as defined in Fig. 5. These results provided some first insight into the spatial depth of the cluster. In order to get a better understanding of the galaxy distribution in the cluster core, Jerjen (2003) determined SBF distances to eight dEs and found a mean distance of $(m-M)_0=31.54\pm0.07\,\mathrm{mag}$, or $20.3\pm0.7\,\mathrm{Mpc}$ and a cluster depth of $\sigma_{\mathrm{int}}=1.4^{+0.5}_{-0.8}\,\mathrm{Mpc}$. The former value was in good agreement with previous SBF work on 26 Fornax E/S0, Sa giants $(31.50\pm0.04\,\mathrm{mag}$, Tonry et al. 2001) spread over a larger cluster area.

With the availability of SBF distances for a total of 43 early-type galaxies (including the 10 dEs from this study) we have the first-time luxury to conduct a 3-D Fornax cluster analysis right in the cluster center. Fig. 6 shows three different representations of the distance distribution of the 31 dE+E galaxies that are in projection closer than three core radii (2°) from NGC1399. This sample size is equivalent to 35 percent of all early-type galaxies in the Fornax Cluster Catalog brighter than $-13.5 \,\mathrm{mag}$ located in that area. The top panel is the histogram, binned in 0.1 mag bins. The second panel uses the adaptive kernel method (Vio et al. 1994) with a Gaussian kernel. Interestingly, both graphs show evidence for two or even three concentrations, the two major ones centered at a distance modulus of \approx 31.3 and at just under 31.6. The bottom panel is probably the closest to reality showing the distribution using the adaptive kernel method and adopting an average SBF distance uncertainty of 0.2 mag. The process completely straightens out the substructure indicating that the number of galaxies and the accuracy in the distance measurements are not sufficient to establish the reality of this effect. Nevertheless, the concentrations in the distribution of the individual galaxies still stand out and should be tested in future studies. The selected 31 dE+E galaxies give a preliminary distance of $19.95\pm0.37\,\mathrm{Mpc}\,[(m-M)_0=31.49\pm0.04\,\mathrm{mag}]$ to the Fornax cluster core. A final value will be given in §4.3.

Next we wish to investigate the line-of-sight cluster depth to further reduce the uncertainties in the Jerjen (2003) result. The observed dispersion in the distance distribution of

our sample galaxies, $\sigma_{(m-M)} = 0.24 \,\mathrm{mag}$ is influenced by two factors: the distance errors and the intrinsic cluster depth. The depth can be calculated via: $\sigma_{\mathrm{los}}^2 = \sigma_{(m-M)}^2 - \sigma_{\Delta(m-M)}^2$, where $\sigma_{\Delta(m-M)}$ must be a representative estimate of the distance errors. Because the distance accuracy of our sample shows quite some variation we generated 100,000 bootstrap samples (Efron & Tibshirani 1986) of distances and errors from the original data set. For each sample we calculated its mean distance and mean error and used the previous equation to determine σ_{los} . Histograms were then produced for all three parameters, each well approximated by a Gaussian. The σ_{los}^2 distribution was found to peak at 0.0075 with a 1σ scatter of 0.0105. This translates into a true line-of-sight cluster depth of $\sigma_{\mathrm{int}} = 0.74^{+0.52}_{-0.74} \,\mathrm{Mpc}$ which is in good agreement with the small linear extension of Fornax in the sky as estimated from the positions of early-type galaxies in the FCC: $\sigma_{\mathrm{R.A.}} = 0.55 \pm 0.06 \,\mathrm{Mpc}$; $\sigma_{\mathrm{DEC}} = 0.46 \pm 0.05 \,\mathrm{Mpc}$. We conclude that the early-type galaxy population in the central region of the Fornax cluster is spatially well constrained with no evidence of elongation along the line-of-sight.

4.2. The Hubble diagram

Unlike previous work (e.g. Drinkwater et al. 2001a) that concentrated on measuring global kinematical properties of the Fornax cluster we now have velocities and distances available for 29 early-type galaxies within a 2 degree (720 kpc) radius from NGC1399, a data set highly suitable for analysing gravitationally induced motion right in the core of the Fornax cluster. The velocity-distance diagram for these galaxies is shown in Fig.7.

On the near side, almost all galaxies (9 out of 12) with distance estimates closer than the tentative cluster center are redshifted relative to the cosmological expansion. Only the three galaxies NGC1386, FCC222, and FCC278 stand out as they appear isolated in the velocity-distance space. They are blueshifted by $\approx 360\,\mathrm{km\,s^{-1}}$ relative to the Hubble flow and $\approx 700\,\mathrm{km\,s^{-1}}$ to the the other sample galaxies at comparable distances. The main galaxy in the ensemble, NGC1386, whose SBF distance was measured by Tonry et al. (2001), is a Sa galaxy hosting a Seyfert 2 nucleus (Weaver et al. 1991). FCC222 was classified as a SAB(s)0 galaxy but no evidence for a disk or spiral features was found in our high resolution FORS1 images. Hence, the morphological type "dE0,N" as initially given in the Fornax cluster catalogue (Ferguson 1989) must be considered to be a more accurate description.

The situation in the Hubble diagram is equally pronounced on the far side of the cluster. With only two and possibly a third exception all galaxies are blueshifted to the systemic velocity. Those are NGC1404 together with NGC1382 and the dwarf FCC100. NGC1404 is a well known object in the X-ray community (Jones et al. 1997; Machacek et al. 2005). The X-ray emission of NGC1404 shows a distorted envelope towards NGC1399, suggesting

that NGC1404, which has a similar distance as NGC1399 but a very different velocity, experiences ram pressure stripping of the galaxy gas, caused by its relative motion of $\Delta v = 544 \,\mathrm{km \, s^{-1}}$ through the surrounding intracluster medium. Furthermore, Drinkwater et al. (2001a) speculated that another galaxy, the irregular NGC1427A at $03^h40^m09.3^s - 35^d37^m28^s$ (J2000) with a velocity $v_{\odot} = 2028 \,\mathrm{km \, s^{-1}}$ may be associated to NGC1404 but no distance is available to clarify this to date.

Overall the bulk of sample galaxies exhibit a prominent S-shaped infall pattern suggesting that Fornax is still in the process of formation during the present epoch through a general collapse. The Hubble line intercepts the kinematically defined curve at a distance of $\approx 19.9\,\mathrm{Mpc}$ right at the location, i.e. distance and velocity, of NGC1399 thereby highlighting the central role of this galaxy in the cluster. Based on the prescription of Tully & Shaya (1984) we used a point mass model to estimate the total cluster mass. Adopting 13.7 Gyr as the age of the Universe (WMAP, Spergel et al. 2003) we fitted a mass model at the data points. The best-fitting envelope for the line of sight angle of two degrees from the Fornax cluster center is indicated as solid curve in Fig. 7 mapping the extreme model velocity. From the amplitude of 735 km s⁻¹ we get a cluster mass of $2.3\pm0.3\times10^{14}\,\mathrm{M}_{\odot}$ within 720 kpc projected distance from NGC1399. This result is two times larger than the previously estimated Fornax mass by Drinkwater et al. (2001a) based solely on redshifts for early-type galaxies, and approximately 40 times the mass of NGC1399 ($0.6\times10^{13}\,\mathrm{M}_{\odot}$, Jones et al. 1997). The estimated collapse time for the system is $t_{\rm collapse}=2.9^{+1.6}_{-0.9}\,\mathrm{Gyr}$.

4.3. Fornax cluster distance and the Hubble constant

To determine the physically most meaningful distance to the Fornax cluster we need to remove the six outlying galaxies. The remaining selection of 23 early-type galaxies within a 2 degree radius of NGC1399 that follow the overall infall pattern of the cluster yields a true cluster distance of $20.13 \pm 0.40 \,\mathrm{Mpc}$ [$(m-M)_0=31.51 \pm 0.04 \,\mathrm{mag}$]. This value shall now be used to estimate the Hubble constant. The standard procedure is to transform the mean velocity for the sample galaxies, $1447 \pm 66 \,\mathrm{km \, s^{-1}}$, to the frame of the cosmic microwave background. This required two corrections: (i) a correction of $-115 \pm 18 \,\mathrm{km \, s^{-1}}$ from heliocentric to the barycenter of the Local Group (Courteau & van den Bergh 1999), and (ii) a projected Virgocentric flow correction of $-54 \pm 9 \,\mathrm{km \, s^{-1}}$ in the direction of Fornax. The latter is based on the distance geometry and a 1/R flow-field characteristics of the Local Group-Virgo-Fornax system as outlined in Madore et al. (1999) and the assumption of an infall velocity of $240 \pm 40 \,\mathrm{km \, s^{-1}}$ of the Local Group into the Virgo cluster (Jerjen & Tammann 1993). Finally we use the derived cosmological expansion velocity $v_{CMB}^{Fornax} = 1278 \pm 69 \,\mathrm{km \, s^{-1}}$

to compute the Hubble constant of $63 \pm 5 \,\mathrm{km\ s^{-1}\ Mpc^{-1}}$. We find good agreement with the values derived from various independent techniques such as Cepheid stars by the HST "Key Project" team $(72 \pm 8 \,\mathrm{km\ s^{-1}\ Mpc^{-1}})$, Freedman et al. 2001), the Cosmic Microwave Background by the WMAP team $(73 \pm 3 \,\mathrm{km\ s^{-1}\ Mpc^{-1}})$, and galaxy clusters in the local Universe $(69 \pm 5 \,\mathrm{km\ s^{-1}\ Mpc^{-1}})$, Giovanelli et al. 1997).

5. Summary

In a few years time, HST will cease operation while the launch date for the next generation space telescope JWST is still uncertain. Without a facility to resolve galaxies into stars, the importance of the tip of the red giant branch method as extragalactic distance indicator will fade quickly. That situation will herald a new era for the surface brightness fluctuation method. Imaging surveys with wide-field cameras at optical and near-IR telescopes will cover large areas of sky that can be analysed with the SBF method to measure distances to thousands of early-type galaxies in a similar fashion as redshift surveys are carried out today. To prepare for that opportunity we are developing SAPAC, a fast and semi-automated SBF reduction software package.

We employed SAPAC to process B and R-band VLT+FORS1 images of 10 dE galaxies that were proposed members of the Fornax cluster. The SBF distances confirm membership for all systems. We combined our results with SBF distances and velocities available for other Fornax dE+E galaxies to investigate the innermost region of the cluster. The derived Hubble diagram for 29 early-type galaxies closer than three cluster core radii (2°) from the central galaxy NGC1399 exhibits a pronounced S-shaped infall pattern suggesting that Fornax is dynamically young in a phase of general collapse and possible accretion of a few individual galaxies. A cluster mass model gives the Fornax cluster mass of $2.3\pm0.3\times10^{14}\mathcal{M}_{\odot}$ (within 720 kpc projected distance from NGC1399) and the associated dynamical collapse time is $t_{\text{collapse}} = 2.9^{+1.6}_{-0.9} \,\text{Gyr}$. A kinematically cleaned galaxy subsample then yielded the true distance of the Fornax cluster core at $20.13\pm0.40\,\mathrm{Mpc}$ [$(m-M)_0=31.51\pm0.04\,\mathrm{mag}$]. Applying a bootstrap resampling technique on the distance distribution further reveals a cluster depth of $\sigma_{\rm int} = 0.74^{+0.52}_{-0.74} \,\mathrm{Mpc}$ consistent with the linear extension of the cluster in R.A. and DEC. We conclude that the early-type galaxy population in the Fornax cluster is spatially well constrained by a spherical shape with a characteristic radius of ≈ 0.6 Mpc and we find marginal evidence for some spatial clumping. Combining the cosmological velocity of Fornax and the distance from the kinematically cleansed central cluster sample yields a Hubble constant of $H_0 = 63 \pm 5 \text{ km s}^{-1} \text{ Mpc}^{-1}$.

The authors thank the referee for carefully reading our manuscript and making helpful suggestions to improve our original paper. They are also grateful to the anonymous ESO service observers at the VLT for obtaining the excellent quality images that were essential for this study.

REFERENCES

Ajhar, E. A., & Tonry, J. L. 1994, ApJ, 429, 557

Bertelli, G., Bressan, A., Chiosi, C., Fagotto, F., & Nasi, E. 1994, A&AS, 106, 275

Binggeli, B., & Cameron, L. M. 1991, A&A, 252, 27

Binggeli, B., & Jerjen, H. 1998, A&A, 333, 17

Binggeli, B., Sandage, A., & Tammann, G. A. 1985, AJ, 90, 1681

Binggeli, B., Tammann, G. A., & Sandage, A. 1987, AJ, 94, 251

Caldwell, N., Armandroff, T. E., Da Costa, G. S., & Seitzer, P. 1998, AJ, 115, 535

Courteau, S., & van den Bergh, S. 1999, AJ, 118, 337

Da Costa, G. S., & Armandroff, T. E. 1990, AJ, 100, 162

Drinkwater, M. J., & Gregg, M. D. 1998, MNRAS, 296, L15+

Drinkwater, M. J., Gregg, M. D., & Colless, M. 2001a, ApJ, 548, L139

Drinkwater, M. J., Gregg, M. D., Holman, B. A., & Brown, M. J. I. 2001b, MNRAS, 326, 1076

Efron, B., & Tibshirani, R. 1986, Statistical Science, 1, 54

Ferguson, H. C. 1989, AJ, 98, 367

Ferguson, H. C., & Binggeli, B. 1994, A&A Rev., 6, 67

Ferguson, H. C., & Sandage, A. 1990, AJ, 100, 1

Freedman, W. L., Madore, B. F., Gibson, B. K., Ferrarese, L., Kelson, D. D., Sakai, S., Mould, J. R., Kennicutt, R. C., Ford, H. C., Graham, J. A., Huchra, J. P., Hughes, S. M. G., Illingworth, G. D., Macri, L. M., & Stetson, P. B. 2001, ApJ, 553, 47

Giovanelli, R., Haynes, M. P., da Costa, L. N., Freudling, W., Salzer, J. J., & Wegner, G. 1997, ApJ, 477, L1+

Hanuschik, R., & Silva, D. 2002, The Messenger, 108, 4

Harris, W. E., Durrell, P. R., Pierce, M. J., & Secker, J. 1998, Nature, 395, 45

Hilker, M., Infante, L., Vieira, G., Kissler-Patig, M., & Richtler, T. 1999, A&AS, 134, 75

Jensen, J. B., Luppino, G. A., & Tonry, J. L. 1996, ApJ, 468, 519

Jensen, J. B., Tonry, J. L., & Luppino, G. A. 1998, ApJ, 505, 111

Jerjen, H. 2003, A&A, 398, 63

Jerjen, H. 2005, in Near-Field Cosmology with Dwarf Elliptical Galaxies', Proceedings of IAU Colloquium No. 198, ed. H. Jerjen & B. Binggeli, 322–330

Jerjen, H., Binggeli, B., & Barazza, F. D. 2004a, AJ, 127, 771

Jerjen, H., Binggeli, B., & Freeman, K. C. 2000a, AJ, 119, 593

Jerjen, H., & Dressler, A. 1997, A&AS, 124, 1

Jerjen, H., Freeman, K. C., & Binggeli, B. 1998, AJ, 116, 2873

—. 2000b, AJ, 119, 166

Jerjen, H., Rekola, R., Takalo, L., Coleman, M., & Valtonen, M. 2001, A&A, 380, 90

Jerjen, H., & Tammann, G. A. 1993, A&A, 276, 1

Jerjen, H., Tully, B., & Trentham, N. 2004b, Publications of the Astronomical Society of Australia, 21, 356

Jones, C., Stern, C., Forman, W., Breen, J., David, L., Tucker, W., & Franx, M. 1997, ApJ, 482, 143

Jordán, A., & Null, . 2005, in IAU Colloq. 198: Near-fields cosmology with dwarf elliptical galaxies, ed. H. Jerjen & B. Binggeli, 368–369

Joye, W. A., & Mandel, E. 2003, in ASP Conf. Ser. 295: Astronomical Data Analysis Software and Systems XII, 489—+

- Karachentsev, I. D., Karachentseva, V. E., Dolphin, A. E., Geisler, D., Grebel, E. K., Guhathakurta, P., Hodge, P. W., Sarajedini, A., Seitzer, P., & Sharina, M. E. 2000, A&A, 363, 117
- Karachentsev, I. D., Karachentseva, V. E., Huchtmeier, W. K., & Makarov, D. I. 2004, AJ, 127, 2031
- Karachentsev, I. D., Karachentseva, V. E., Richter, G. M., & Vennik, J. A. 1995, A&A, 296, 643
- Karachentsev, I. D., Sharina, M. E., Dolphin, A. E., & Grebel, E. K. 2003, A&A, 408, 111
- Karachentsev, I. D., Sharina, M. E., Grebel, E. K., Dolphin, A. E., Geisler, D., Guhathakurta, P., Hodge, P. W., Karachentseva, V. E., Sarajedini, A., & Seitzer, P. 1999, A&A, 352, 399
- Kraan-Korteweg, R. C., & Tammann, G. A. 1979, Astronomische Nachrichten, 300, 181
- Landolt, A. U. 1992, AJ, 104, 340
- Machacek, M., Dosaj, A., Forman, W., Jones, C., Markevitch, M., Vikhlinin, A., Warmflash, A., & Kraft, R. 2005, ApJ, 621, 663
- Madore, B. F., Freedman, W. L., Silbermann, N., Harding, P., Huchra, J., Mould, J. R., Graham, J. A., Ferrarese, L., Gibson, B. K., Han, M., Hoessel, J. G., Hughes, S. M., Illingworth, G. D., Phelps, R., Sakai, S., & Stetson, P. 1999, ApJ, 515, 29
- Mei, S., Blakeslee, J. P., Tonry, J. L., Jordán, A., Peng, E. W., Côté, P., Ferrarese, L., West, M. J., Merritt, D., & Milosavljević, M. 2005, ApJ, 625, 121
- Mieske, S., & Hilker, M. 2003, A&A, 410, 445
- Miller, B. W., Lotz, J. M., Ferguson, H. C., Stiavelli, M., & Whitmore, B. C. 1998, ApJ, 508, L133
- Mould, J. R., Hughes, S. M. G., Stetson, P. B., Gibson, B. K., Huchra, J. P., Freedman, W. L., Kennicutt, R. C., Bresolin, F., Ferrarese, L., Ford, H. C., Graham, J. A., Han, M., Hoessel, J. G., Illingworth, G. D., Kelson, D. D., Macri, L. M., Madore, B. F., Phelps, R. L., Prosser, C. F., Rawson, D., Saha, A., Sakai, S., Sebo, K. M., Silbermann, N. A., & Turner, A. M. 2000, ApJ, 528, 655
- Neilsen, E. H., & Tsvetanov, Z. I. 2000, ApJ, 536, 255
- Peebles, P. J. E., Phelps, S. D., Shaya, E. J., & Tully, R. B. 2001, ApJ, 554, 104

Peng, C. Y., Ho, L. C., Impey, C. D., & Rix, H.-W. 2002, AJ, 124, 266

Rekola, R., Jerjen, H., & Flynn, C. 2005, A&A, 437, 823

Schlegel, D. J., Finkbeiner, D. P., & Davis, M. 1998, ApJ, 500, 525

Schmidt, K.-H., & Boller, T. 1992, Astronomische Nachrichten, 313, 329

Schröder, A., Drinkwater, M. J., & Richter, O.-G. 2001, A&A, 376, 98

Silbermann, N. A., Harding, P., Ferrarese, L., Stetson, P. B., Madore, B. F., Kennicutt,
R. C., Freedman, W. L., Mould, J. R., Bresolin, F., Ford, H., Gibson, B. K., Graham,
J. A., Han, M., Hoessel, J. G., Hill, R. J., Huchra, J., Hughes, S. M. G., Illingworth,
G. D., Kelson, D., Macri, L., Phelps, R., Rawson, D., Sakai, S., & Turner, A. 1999,
ApJ, 515, 1

Solanes, J. M., Sanchis, T., Salvador-Solé, E., Giovanelli, R., & Haynes, M. P. 2002, AJ, 124, 2440

Spergel, D. N., Verde, L., Peiris, H. V., Komatsu, E., Nolta, M. R., Bennett, C. L., Halpern,
M., Hinshaw, G., Jarosik, N., Kogut, A., Limon, M., Meyer, S. S., Page, L., Tucker,
G. S., Weiland, J. L., Wollack, E., & Wright, E. L. 2003, ApJS, 148, 175

Thomsen, B., Baum, W. A., Hammergren, M., & Worthey, G. 1997, ApJ, 483, L37+

Tonry, J., & Schneider, D. P. 1988, AJ, 96, 807

Tonry, J. L., Dressler, A., Blakeslee, J. P., Ajhar, E. A., Fletcher, A. B., Luppino, G. A., Metzger, M. R., & Moore, C. B. 2001, ApJ, 546, 681

Tully, R. B., & Shaya, E. J. 1984, ApJ, 281, 31

Tully, R. B., Somerville, R. S., Trentham, N., & Verheijen, M. A. W. 2002, ApJ, 569, 573

Vio, R., Fasano, G., Lazzarin, M., & Lessi, O. 1994, A&A, 289, 640

Weaver, K. A., Wilson, A. S., & Baldwin, J. A. 1991, ApJ, 366, 50

West, M. J., & Blakeslee, J. P. 2000, ApJ, 543, L27

Worthey, G. 1994, ApJS, 95, 107

This preprint was prepared with the AAS IATEX macros v5.2.

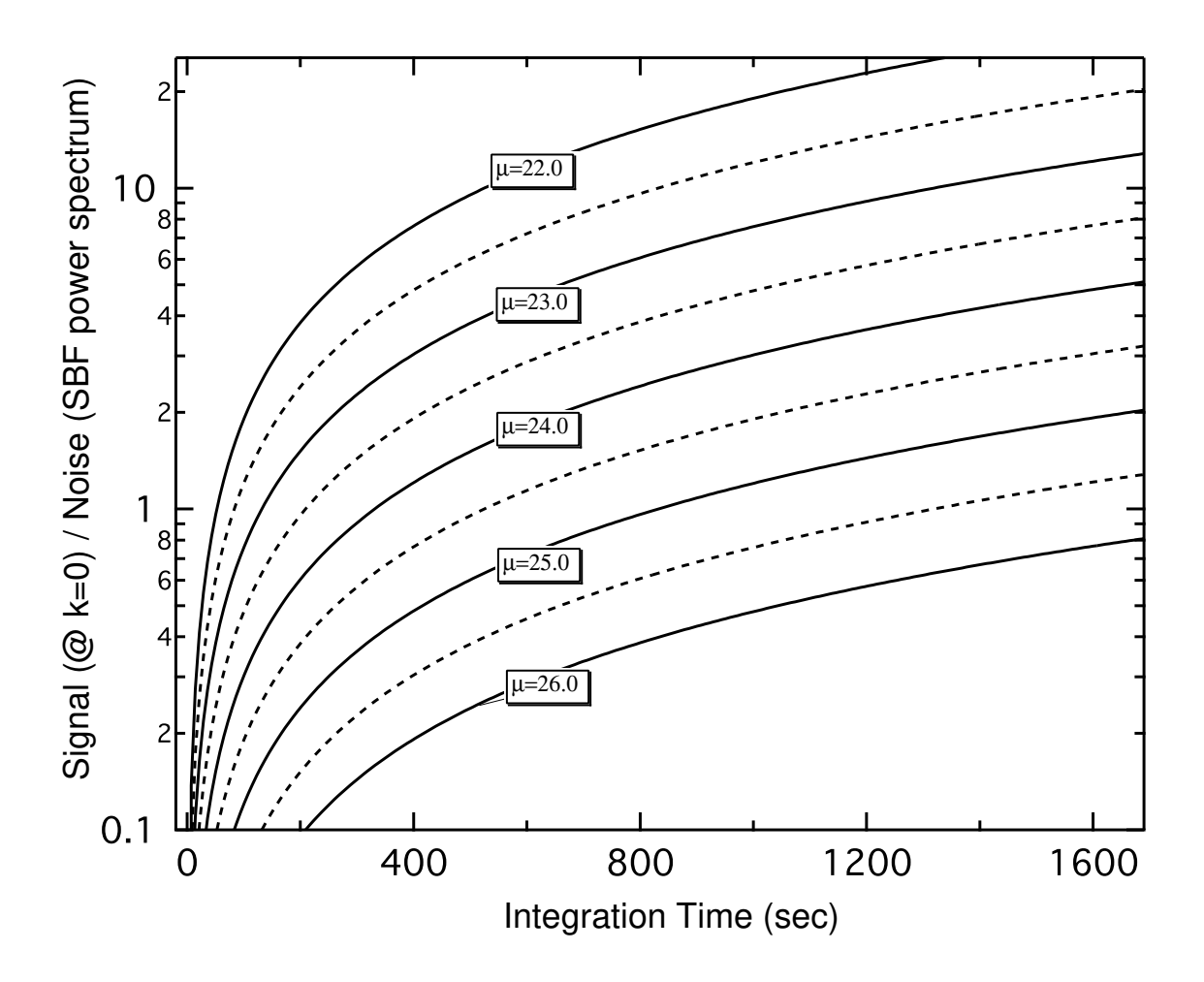


Fig. 1.— An illustration showing how the signal-to-noise in the SBF power spectrum increases with length of exposure time and galaxy surface brightness at the adopted distance modulus of 31.50 mag. The modeled telescope is the VLT+FORS1 with a photometric zero point of $m_{1,R} = 27.10$ mag and a sky brightness of $\mu_{sky,R} = 20.8$ mag arcsec⁻². The surface brightness fluctuation luminosity is set at $\overline{M}_R = -1.30$ mag.

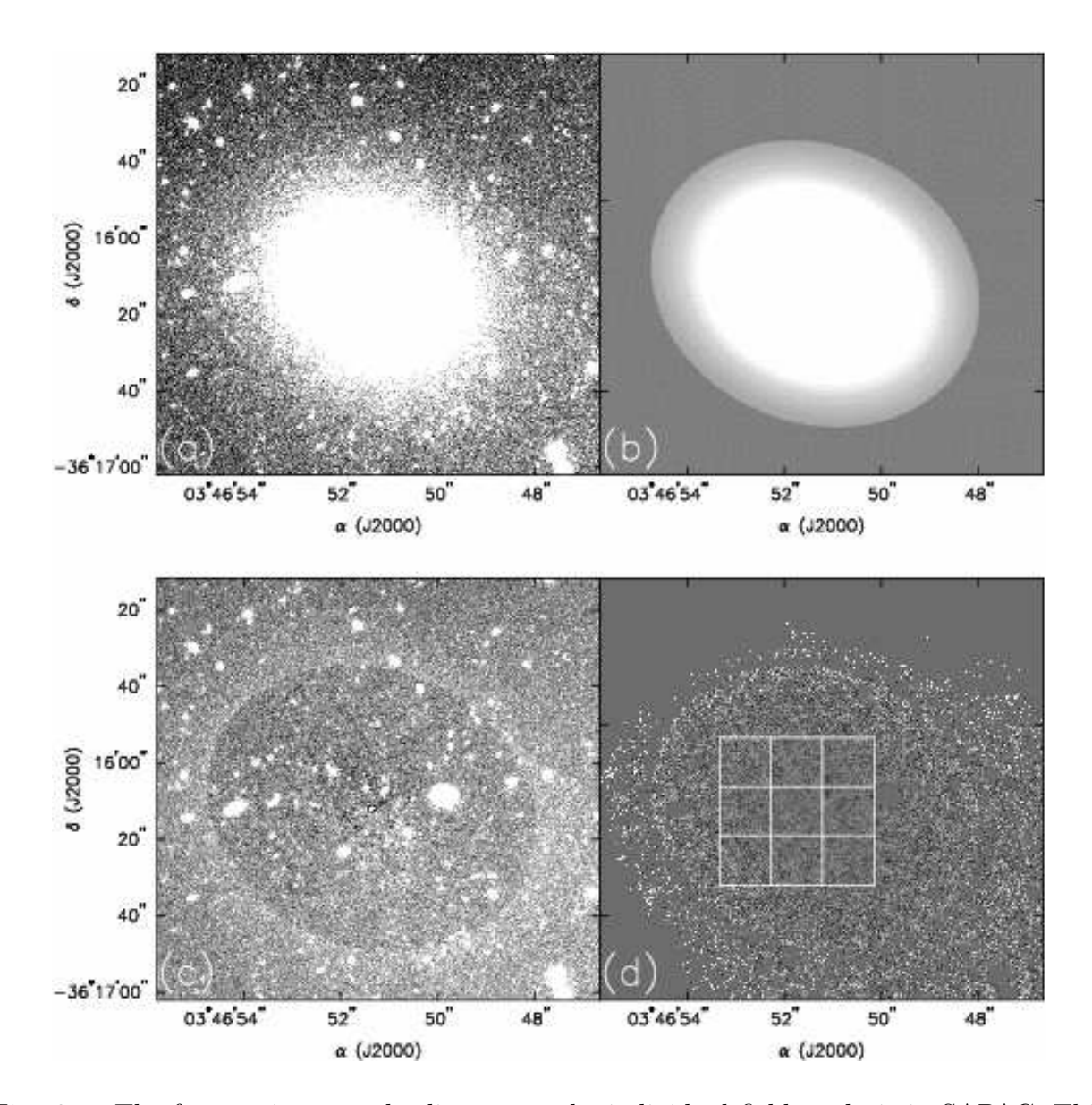


Fig. 2.— The four major steps leading up to the individual field analysis in SAPAC. This example shows FCC318. (top left, a) shows the original FORS1 R-band image of the galaxy; (top right, b) the best-fitting model of the light distribution from SAPAC; (bottom left, c) the residual, after subtraction of the model; (bottom right, d) the final result after normalization, masking and a 3×3 grid is overlaid. The mottling of the unresolved stars in the galaxy center is clearly visible.

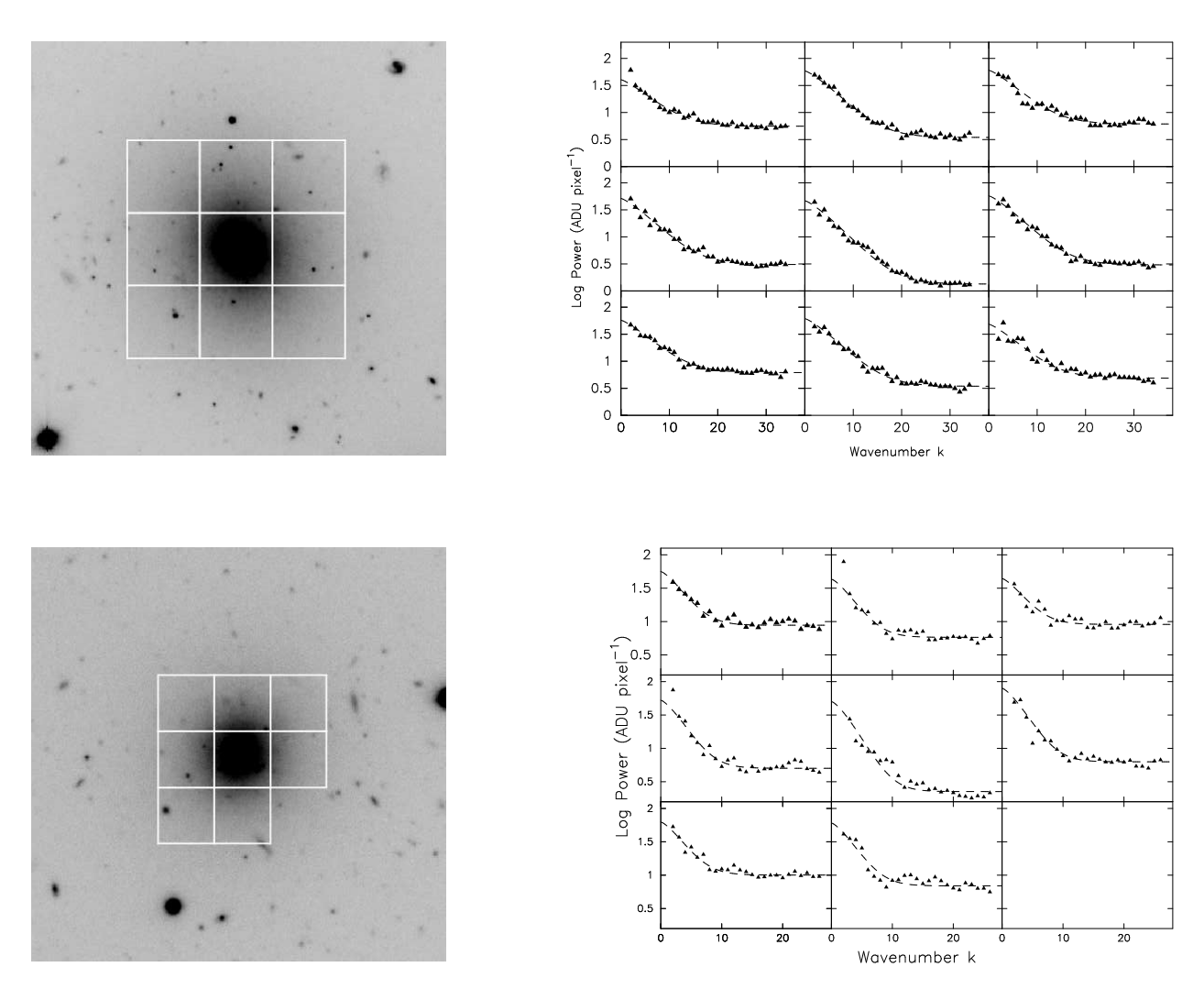


Fig. 3.— *R*-band images for the galaxies FCC222 (top) and FCC243 (bottom) with the grid of user-selected SBF fields superimposed. The corresponding power spectra are shown on the right. The observational data (triangles) are best fitted by the sum of a scaled version of the PSF power spectrum and a constant (dashed line).

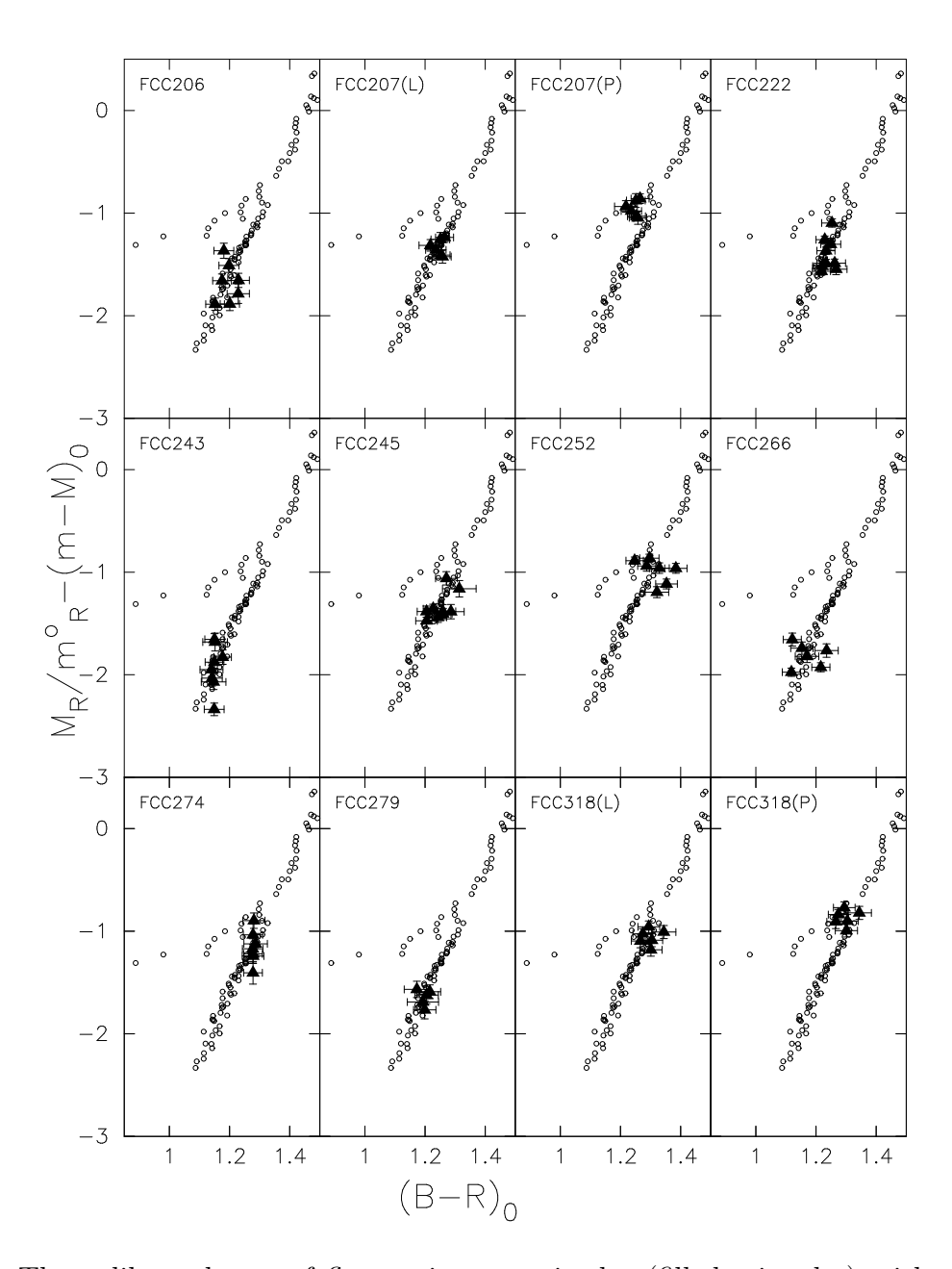


Fig. 4.— The calibrated sets of fluctuation magnitudes (filled triangles) with error bars for the ten Fornax dEs analysed. The open circles are the 170 data points that define the semi-empirical calibration (see Jerjen 2005). In two cases (FCC207 and FCC318) results for both branches (labeled "L" for linear and "P" for parabolic) are shown as we could not confidently discard one of the two possible results. For the distance values see Table 6.

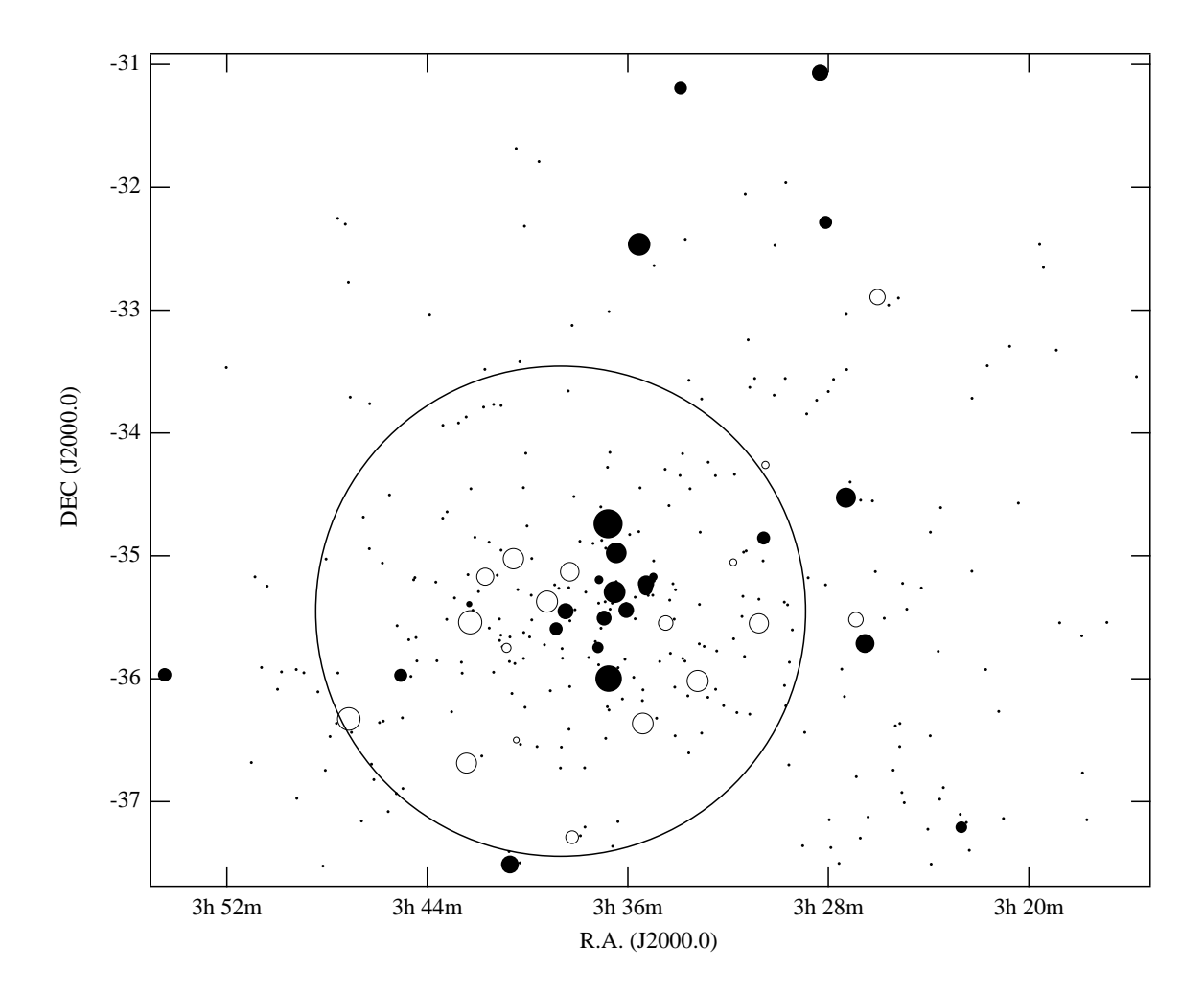


Fig. 5.— The galaxy distribution in the Fornax cluster based on the Fornax Cluster Catalog (Ferguson 1989). All galaxies are shown as dots except the 43 early-type galaxies with available SBF distance measurements. The symbol size is inversely proportional to the galaxy distance. Dwarfs are open and giants are filled circles. The cluster core region is highlighted with a circle centered at NGC1399 and of radius two degrees equivalent to three cluster core radii or 720 kpc.

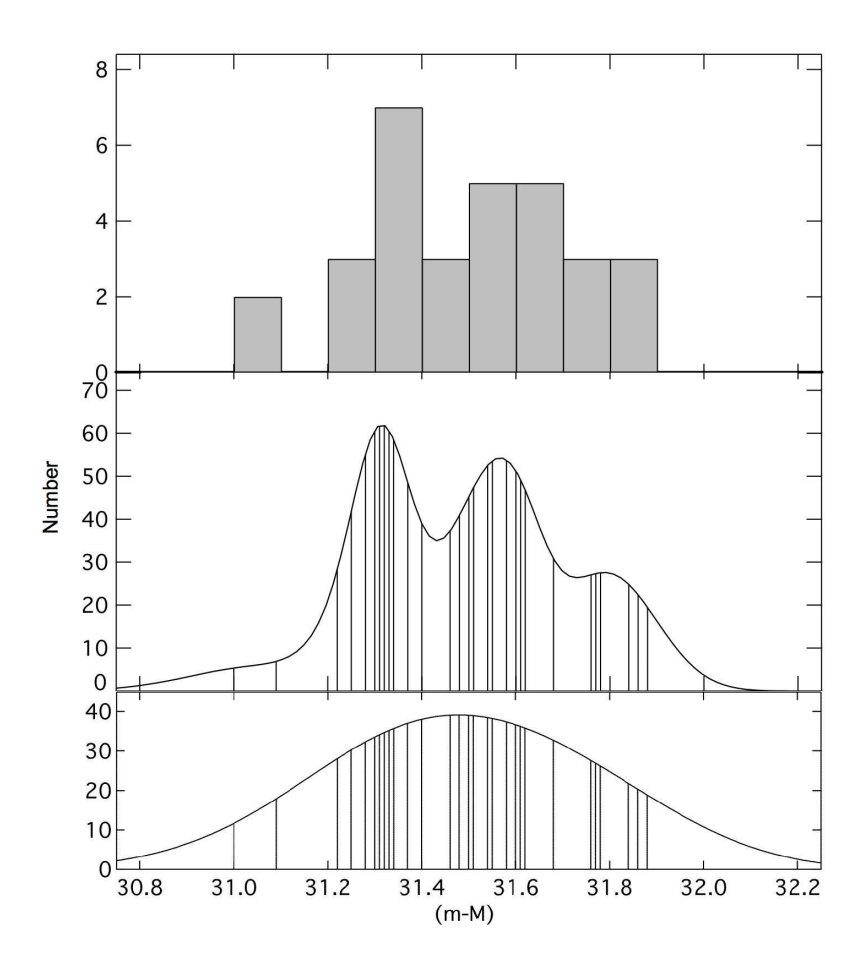


Fig. 6.— The top figure shows a histogram of the distance distribution of the 31 dE+E galaxies within 2 degrees ($720\,\mathrm{kpc}$) radius of NGC1399 with SBF distances from our studies and the literature. The second panel used an adaptive kernel method to test for substructure. The vertical lines apply to the individual galaxies used in this analysis. The third panel also used an adaptive kernel but adopts a $0.2\,\mathrm{mag}$ average error and this appears to smooth the previously apparent substructure out.

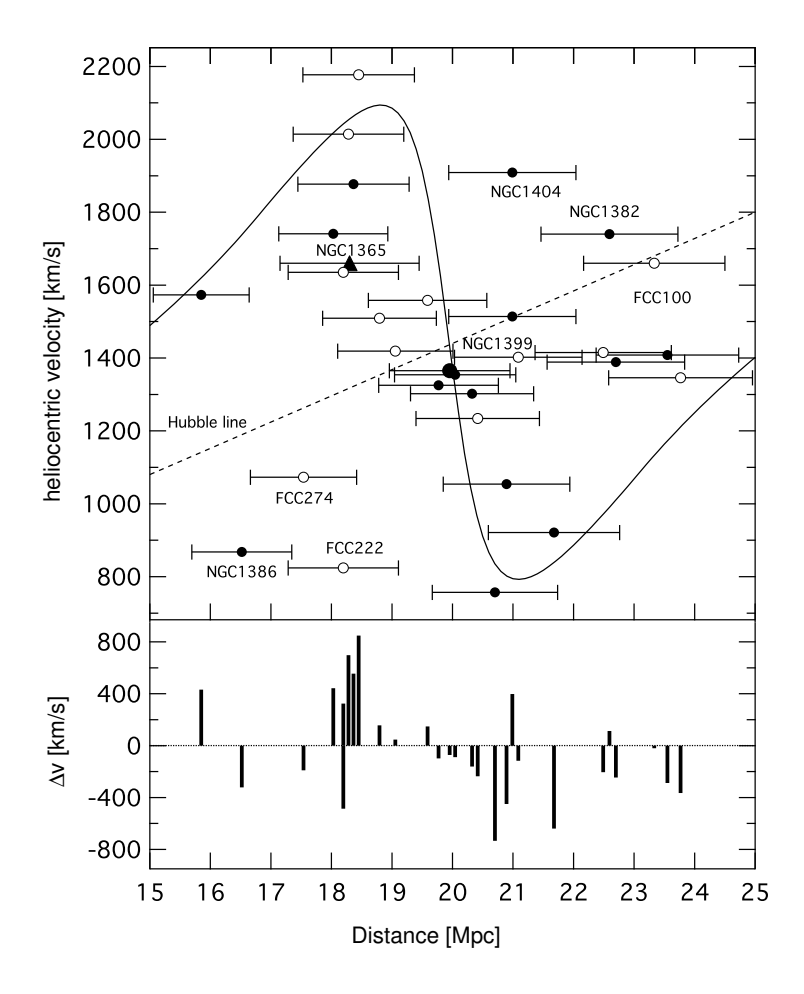


Fig. 7.— Top: Velocity-distance diagram for 29 dE+E galaxies from the central Fornax cluster region. Open circles refer to dwarf ellipticals, filled circles represent giant ellipticals. Error bars correspond to 0.5σ distance uncertainty. The Hubble line is indicated as a dashed line and the solid S-curve represents the best-fitting mass-age cluster model. Peculiar velocities are plotted relative to the Hubble expansion. For further discussion see text. The spiral galaxy NGC1365 that is located in the central cluster area and has a Cepheids distance is shown as a filled triangle. Bottom: Individual galaxy peculiar velocities are plotted as a function of distance.

Table 1. Basic properties of the observed early-type dwarf galaxies in the Fornax cluster.

FCC (1)	Type (2)	R.A. (J2000.0) (3)	Decl. (J2000.0) (4)	$B_T \pmod{5}$	$v_{\odot} \ (\text{km s}^{-1})$ (6)	$A_B $ (mag) (7)	$A_R $ (mag) (8)
206	dE0pec	03h38m13.4s	-37d17m18s	15.8	1402*	0.061	0.038
207	$_{ m dE2,N}$	$03\mathrm{h}38\mathrm{m}16.2\mathrm{s}$	$-37\mathrm{d}07\mathrm{m}39\mathrm{s}$	15.9	1419*	0.063	0.039
222	$_{ m dE0,N}$	$03\mathrm{h}39\mathrm{m}13.3\mathrm{s}$	$-35\mathrm{d}22\mathrm{m}11\mathrm{s}$	15.6	953^{\ddagger}	0.056	0.035
243	$_{ m dE1,N}$	$03\mathrm{h}40\mathrm{m}26.9\mathrm{s}$	$-36\mathrm{d}29\mathrm{m}51\mathrm{s}$	16.5	1404*	0.047	0.029
245	$_{ m dE0,N}$	$03\mathrm{h}40\mathrm{m}33.7\mathrm{s}$	-35d01m17s	16.0	2124*	0.051	0.032
252	$_{ m dE0,N}$	$03\mathrm{h}40\mathrm{m}50.2\mathrm{s}$	$-35\mathrm{d}44\mathrm{m}49\mathrm{s}$	16.0	1415*	0.045	0.028
266	$_{ m dE0,N}$	$03\mathrm{h}41\mathrm{m}41.2\mathrm{s}$	$-35\mathrm{d}10\mathrm{m}08\mathrm{s}$	15.9	1551^{*}	0.045	0.028
274	$_{ m dE0,N}$	$03\mathrm{h}42\mathrm{m}17.1\mathrm{s}$	$-35\mathrm{d}32\mathrm{m}21\mathrm{s}$	16.5	1073^{\dagger}	0.050	0.031
279	$_{ m dE0,N}$	$03\mathrm{h}42\mathrm{m}26.2\mathrm{s}$	$-36\mathrm{d}41\mathrm{m}09\mathrm{s}$	16.7	_	0.032	0.02
318	$_{ m dE2,N}$	$03\mathrm{h}47\mathrm{m}08.0\mathrm{s}$	$-36\mathrm{d}19\mathrm{m}32\mathrm{s}$	16.1		0.051	0.032

References. — * Drinkwater et al. (2001b), \ddagger Ferguson (1989), \dagger Hilker et al. (1999). All data in columns 7 & 8 from Schlegel et al. (1998). All data in columns 1, 2 and 5 from Ferguson (1989)

Table 2. Observing log of the imaging data taken in service mode.

FCC (1)	Filter (2)	UT Date (3)	Mean Airmass (4)	Exptime (sec) (5)	FWHM (arcsec) (6)	Filter (7)	UT Date (8)	Mean Airmass (9)	Exptime (sec) (10)	FWHM (arcsec) (11)
206	B	2001-11-20	1.03	3x500	0.69	R	2002-08-13	1.29	3x700	0.55
207	B	2001-11-20	1.02	3x500	0.52	R	2002-08-13	1.16	3x700	0.62
222	B	2001-12-07	1.02	3x500	0.91	R	2002-08-13	1.09	3x700	0.58
243	B	2001-12-07	1.03	3x500	0.82	R	2002-08-14	1.36	3x700	0.69
245	B	2001-12-07	1.05	3x500	0.79	R	2003-08-07	1.03	6x700	0.69
252	B	2001-12-11	1.10	3x500	0.79	R	2003-09-06	1.02	3x700	0.55
266	B	2001-12-11	1.18	3x500	0.98	R	2003-08-06	1.12	3x700	0.70
274	B	2002-01-15	1.02	3x500	0.85	R	2003-08-31	1.01	1x700	0.56
279	B	2002-01-12	1.02	3x500	0.94	R	2003-09-29	1.34	3x700	0.79
318	B	2001-11-18	1.12	3x500	0.72	R	2003-09-30	1.02	3x700	0.57

Table 3. Photometric parameters for each observing night

UT Date (1)	k_B (2)	k_R (3)	$C_{B-R} \tag{4}$	ZP (5)
(1)	(2)	(0)	(4)	(9)
2001-11-18	0.27	0.12	-0.054	$27.069 \pm (0.010)(B)$
2001-11-20	0.27	0.12	-0.054	$27.055 \pm (0.005)(B)$
2001-12-07	0.29	0.12	-0.060	$27.038 \pm (0.011)(B)$
2001-12-11	0.29	0.12	-0.060	$27.119 \pm (0.005)(B)$
2002-01-12	0.30	0.13	-0.066	$27.058 \pm (0.004)(B)$
2002 - 01 - 15	0.30	0.13	-0.066	$27.024 \pm (0.005)(B)$
2002-08-13	0.21	0.07	-0.048	$27.210 \pm (0.006)(R)$
2002-08-14	0.21	0.07	-0.048	$27.266 \pm (0.033)(R)$
2003-08-06	0.24	0.11	-0.067	$27.347 \pm (0.003)(R)$
2003-08-07	0.24	0.11	-0.067	$27.383 \pm (0.002)(R)$
2003-09-01	0.24	0.11	-0.067	$27.163 \pm (0.010)(R)$
2003-09-06	0.24	0.11	-0.067	$27.440 \pm (0.016)(R)$
2003-09-29	0.24	0.11	-0.067	$27.328 \pm (0.006)(R)$
2003-09-30	0.24	0.11	-0.067	$27.342 \pm (0.009)(R)$

Table 4. Parameters of SBF fields in two galaxies

Galaxy Field name	size (pixels)	m_1 (mag)	\overline{g} (ADU)	s (ADU)	$ \begin{array}{c} P_0 \\ \text{(ADU s}^{-1} \text{ pixel}^{-1}) \end{array} $	$ \begin{array}{c} P_1 \\ \text{(ADU s}^{-1} \text{ pixel}^{-1}) \end{array} $	S/N	P_{BG}/P_0
(1)	(2)	(3)	(4)	(5)	(6)	(7)	(8)	(9)
FCC222(1,1)	70	27.11	881.8	9236.7	0.058(0.002)	0.008	5.3	0.04
FCC222(1,2)			1370.2		0.084(0.002)	0.005	10.9	0.03
FCC222(1,3)			718.0		0.087(0.004)	0.009	7.4	0.03
FCC222(2,1)			1587.1		0.074(0.002)	0.004	10.2	0.03
FCC222(2,2)			4629.1		0.067(0.002)	0.002	14.4	0.04
FCC222(2,3)			1587.5		0.082(0.002)	0.004	11.6	0.03
FCC222(3,1)			762.8		0.082(0.002)	0.009	7.0	0.03
FCC222(3,2)			1505.6		0.088(0.003)	0.005	11.5	0.03
FCC222(3,3)			943.7		0.070(0.004)	0.007	7.0	0.04
FCC243(1,1)	54	27.19	543.3	11655.3	0.080(0.004)	0.013	5.0	0.04
FCC243(1,2)			1014.7		0.062(0.003)	0.008	5.2	0.05
FCC243(1,3)			489.6		0.063(0.004)	0.013	3.8	0.05
FCC243(2,1)			1063.8		0.075(0.004)	0.007	7.1	0.04
FCC243(2,2)			2754.7		0.072(0.005)	0.003	11.2	0.04
FCC243(2,3)			815.9		0.114(0.006)	0.009	9.3	0.03
FCC243(3,1)			487.5		0.090(0.005)	0.014	5.0	0.03
FCC243(3,2)			778.2		0.087(0.006)	0.010	6.5	0.03

Table 5. Fluctuation magnitudes and colours for SBF fields in two galaxies

Galaxy	A_{R}	\overline{m}_{R}^{0}	$(B - R)_0$
Field	(mag)	(mag)	(mag)
(1)	(2)	(3)	(4)
FCC222(1,1)	0.03 ± 0.01	30.20 ± 0.04	1.25 ± 0.03
FCC222(1,2)		29.78 ± 0.03	1.22 ± 0.03
FCC222(1,3)		29.75 ± 0.05	$1.27{\pm}0.04$
FCC222(2,1)		29.93 ± 0.03	1.23 ± 0.03
FCC222(2,2)		30.04 ± 0.04	1.23 ± 0.03
FCC222(2,3)		29.81 ± 0.04	1.23 ± 0.03
FCC222(3,1)		29.81 ± 0.04	$1.26 {\pm} 0.04$
FCC222(3,2)		29.73 ± 0.04	1.22 ± 0.03
FCC222(3,3)		29.99 ± 0.06	$1.25 {\pm} 0.03$
FCC243(1,1)	0.03 ± 0.01	29.93 ± 0.07	$1.14 {\pm} 0.04$
FCC243(1,2)		30.22 ± 0.06	1.15 ± 0.03
FCC243(1,3)		30.20 ± 0.09	1.15 ± 0.04
FCC243(2,1)		30.00 ± 0.06	1.15 ± 0.03
FCC243(2,2)		30.05 ± 0.07	1.18 ± 0.03
FCC243(2,3)		29.54 ± 0.06	1.15 ± 0.03
FCC243(3,1)		$29.81 {\pm} 0.07$	$1.15 {\pm} 0.04$
FCC243(3,2)		$29.85 {\pm} 0.08$	1.14 ± 0.03

Table 6. SBF distances for the Fornax dwarf ellipticals with two results listed for undecided cases (linear branch result listed first)

FCC Number	$ (m - M)_0 $ (mag) $ 2 $	D (Mpc) 3
206 207 222 243 245 252 266 274 279 318	31.62 ± 0.26 31.40 ± 0.13 31.02 ± 0.09 31.30 ± 0.18 31.88 ± 0.22 31.33 ± 0.18 31.76 ± 0.35 31.46 ± 0.33 31.22 ± 0.16 31.34 ± 0.14 31.25 ± 0.18	21.09 ± 2.68 19.05 ± 1.18 16.00 ± 0.67 18.20 ± 1.57 23.77 ± 2.53 18.45 ± 1.59 22.49 ± 3.93 19.59 ± 3.21 17.54 ± 1.34 18.54 ± 1.23 17.78 ± 1.54
•••	31.06 ± 0.10	16.29 ± 0.77